Journal of Rock Mechanics and Geotechnical Engineering 17 (2025) 3609–3618

Contents lists available at ScienceDirect

Journal of Rock Mechanics and Geotechnical Engineering

journal homepage: www.jrmge.cn

Full Length Article

A city-wide investigation on the subsurface temperature evolution and geothermal capacity evaluation

Liwei Zhang [a, b], Chun Liu [a, *], Bin Shi [a], Peter Bayer [c], Huan Geng [a]

[a] School of Earth Sciences and Engineering, Nanjing University, Nanjing, 210093, China
[b] Department of Civil Engineering and Environmental Engineering, The Hong Kong University of Science and Technology, Hong Kong, China
[c] Department of Applied Geology, Martin Luther University of Halle-Wittenberg, Halle, Germany

ARTICLE INFO

Article history:
Received 19 February 2024
Received in revised form
2 May 2024
Accepted 28 May 2024
Available online 23 September 2024

Keywords:
Field-monitoring
Satellite temperature correction
Temperature distribution
Geothermal capacity evaluation

ABSTRACT

The subsurface urban heat island (UHI) effect can provide latent clean geothermal potentials for cities. Understanding the city-wide subsurface temperature evolution under different land surfaces is significant in making better use of geothermal energy. This research presents a study of Nanjing to identify the city-wide temperature distribution and evolution characteristics and further estimates the geothermal potential in Nanjing. Low-cost satellite-measured temperatures were used to derive the subsurface temperatures through a liner regression correction method, with higher accuracy verified by measured borehole data. The simulation results indicate that the concrete surface exhibits higher average temperatures than the grassland surface, resulting in relatively higher subsurface temperatures. The deviations of simulated subsurface temperatures are attributed to many factors, including the influence of complex atmospheric conditions on satellite-measured temperature accuracy, land surface heat absorption, and infiltration in the shallower layer. Furthermore, it reveals that the urban areas have 14.7% greater geothermal potential compared to rural areas, due to the subsurface UHI effect. This study provides a potentially efficient and convenient method for the estimation of potential urban geothermal energy.

1. Introduction

Geothermal energy is a new type of renewable, effective, and clean energy with great prospects for future development. The temperature difference between rural and urban areas, which is known as the urban heat island (UHI) effect, poses latent geothermal potential for cities (Zhu et al., 2010; Bayer et al., 2019). Developed geothermal energy, which provides heat for residential, commercial, and public buildings, has been widely applied in many countries during cold days (Lin et al., 2020; Bae and Nam, 2021). Thus, understanding soil temperature evolution features and acquiring temperature distribution are significant to make better use of these heat sources. The usage of the convenient and low-cost satellite-measured temperatures can help evaluate the city-scale geothermal capacity, which is beneficial to the exploitation of the geothermal potential.

Previous research has contributed to a better understanding of spatiotemporal features of ground temperature because of the exploration of geothermal energy. The surface temperature typically performs a sinusoidal curve throughout the year, and there is a lag when the surface temperature transfers into the subsurface, so the temperature amplitude dampens with increasing depth (Stallman, 1965; Taniguchi, 1993; Figura et al., 2015). The subsurface temperature distribution in the shallow layer (about 200 m) generally comprises three distinguished zones, which are the variant zone, the constant zone, and the increased zone. Meanwhile, numerous studies have examined the factors influencing the temperature distribution, such as land covers, air temperature, weather, global warming, and seasons (Popiel and Wojtkowiak, 2013; Balugani et al., 2017; Zou et al., 2021). For instance, Popiel and Wojtkowiak (2013) compared the land cover effect on the temperature distribution and discovered that the average surface temperature of lawns was lower in summer and higher in winter compared with the bare ground. In addition, groundwater significantly affects the subsurface temperatures, with upward and downward-moving groundwater changing the temperature-depth profiles (Taniguchi et al., 2005). Groundwater types impact subsurface temperature as well

* Corresponding author.
E-mail address: chunliu@nju.edu.cn (C. Liu).
Peer review under responsibility of Institute of Rock and Soil Mechanics, Chinese Academy of Sciences.

https://doi.org/10.1016/j.jrmge.2024.05.051

(Taniguchi et al., 2009; Epting and Huggenberger, 2013). As for the geological structures, faults provide a good groundwater pathway for heat circulation and promote the removal of heat flux (Mortimer et al., 2011; Siler et al., 2019). Moreover, the mineral composition affects thermal conductivity and heat capacity, including physical characteristics, such as density, structure, particle size, and others (Dong et al., 2015; Zhang et al., 2018).

Soil temperatures can be acquired from both field measurements and numerical models. Various temperature sensors with an accuracy of about 0.1 K are used to obtain temperature profiles. However, these sensors can only be manually inserted into the point and the spatial resolution is usually 2 m or even coarser (Kurylyk et al., 2014a; Tissen et al., 2020). Conventional monitoring of large-scale sites in the field is labor-intensive because of the uneven temperature distribution, while the use of remote sensing technologies has made large-scale temperature monitoring possible (Yao et al., 2017; Li et al., 2019). Nonetheless, remote sensing datasets can only detect surface temperatures as depth as micrometers, and the precision of the temperature data is difficult to guarantee compared with measured data (Benz et al., 2016; Li and Zha, 2019). Furthermore, numerical models provide an insight to investigate the thermal transferring process (Wang et al., 2023). Numerical methods bring the advantage of predicting the temperature distribution at any time and depth. Subsurface temperatures have been modeled for many conditions, such as analytical and numerical models (Lesperance et al., 2010; Kurylyk et al., 2014b), empirical conduction-advection heat transport equation (Rivera et al., 2015; Des Tombe et al., 2019), and some statistical methods (Herb et al., 2008). Based on these methods, multiple perspectives are presented to study the acquisition method of ground temperatures under multi-factor conditions (Ahmed et al., 2013; Alcaraz et al., 2016; Zhou et al., 2018a).

Ground source heat pump (GSHP) systems, which use renewable geothermal energy to provide heating for residential, commercial, and public buildings, have been widely applied in many countries (Lin et al., 2020; Bae and Nam, 2021). In addition, the geothermal capacity can also be evaluated by using known temperature distributions, which is beneficial for guiding and optimizing the exploitation of geothermal potential.

Despite considerable efforts, obtaining temperature distributions of large-scale districts remains a big challenge because of the complexity of the geological conditions, among other factors (Du et al., 2016; Benz et al., 2018). Thermal remote sensing is an effective means to cope with these difficulties and the produced data has higher credibility (Ahmed et al., 2013). Benz et al. (2017) established the approximate offset relationship between ten years of mean shallow groundwater temperature and satellite-derived land surface temperature by considering the influencing effects of evaporation and snow cover. Zhan et al. (2014) designed a three-time-scale model to derive soil temperatures, which performs annual temperature, daily-averaged temperature, and diurnal temperature variation features. However, the derived temperatures seem not to reflect the actual surface temperatures due to interferences of weather conditions while collecting data from satellite sensors (Zhou et al., 2018b). Additionally, soil properties of the confining layers are not fully considered and the boundary condition is ideal in these methods. The empirical thermal conduction equation provides support for predicting the temperature variations through some records of measured temperatures. Thus, the temperatures and geothermal capacity can be estimated based on some measured surface temperatures and other related variables.

Based on satellite-derived data and field-measured temperatures, this study investigates the surface and subsurface temperature distribution of Nanjing and develops a method to estimate subsurface temperatures. Different means were utilized to acquire surface temperatures and seasonal subsurface temperatures, which may provide important data support for the analysis of temperature distribution and effects. A linear regression model was introduced to correct Moderate Resolution Imaging Spectroradiometer (MODIS) temperatures at sites with land coves of concrete and grassland in Nanjing. Furthermore, the corrected surface temperatures were used as the top boundary condition to simulate subsurface temperatures. Combined with the measured subsurface temperatures, the error and influencing factors of the simulated subsurface temperatures were discussed, including the MODIS data, land cover types, and thermal parameters. Finally, the additional geothermal potential resulting from subsurface UHI effects was evaluated.

2. Study area and methods

In this study, various temperature sensors including the distributed temperature sensor (DTS), iButton, PT100, and thermal remote sensing techniques are applied to acquire continuous surface and seasonal subsurface temperature distribution, under previously established boreholes in Nanjing.

2.1. Study area and monitoring sites

Nanjing (32°03′N, 118°46′E) is located west of Shanghai, China. It covers a total area of 6587.02 km^2 and has a population of approximately 9.3 million. Nanjing has a typical humid subtropical climate and the four seasons are distinct. The mean annual air temperature is 17.1 °C, and the mean annual precipitation is 1032.1 mm (China Meteorological Data Network, 2019). The topography in Nanjing is relatively diverse, with hills, low mountains, and valley plains. The geological structure is also complex including obvious faults and folds in the area. Groundwater resources are rich, with rivers and lakes accounting for 14.4% of the total area, and the main rivers are the Yangtze River, Qinhuai River, and Chu River.

Subsurface temperatures can be measured from some boreholes at a depth of 80–100 m in the long-term observation stations of Nanjing. The locations of these stations are illustrated in Fig. 1. The water levels at these sites are between 2 m and 10 m below ground level. The geological profiles of some representative drillings are depicted in Fig. 2, the shallow subsurface (15–40 m) comprises mostly silty clay and mudstone, and the deeper section (40–100 m) is moderately weathered siltstone and mudstone.

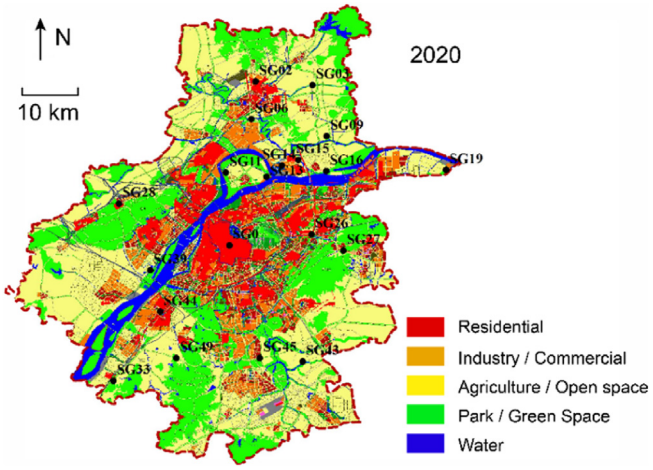

Fig. 1. Locations of the observation stations and the distribution of measurement points.

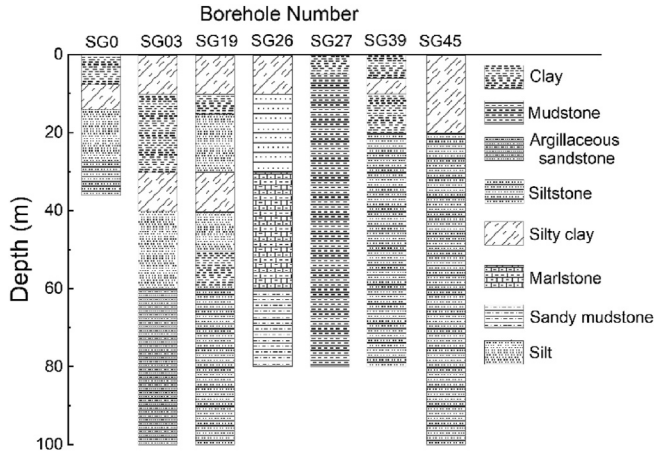

Fig. 2. Sectional histogram of some representative boreholes.

2.2. Field monitoring

2.2.1. Ground surface temperature

Continuous surface temperatures can be recorded and stored at a given time interval via the iButton. The iButton is a small button-shaped sensor, which has a high precision in temperature monitoring (0.1 °C). It has a memory capacity of 64 KB, which may record 4096 temperature data points at a time. The recording interval was set as 1 h, and therefore, it may record temperature data of approximately 170 d. After setting up the sensors through the Enlog software (V3.5.6), they are buried beside the boreholes, below the surface at approximately 0.05 m depth.

2.2.2. Ground subsurface temperature

For subsurface temperature measurements, as shown in Fig. 3a and b, DTS and PT100 were used. A double U-shaped tube was buried in the borehole and the diameter of a single pipe was 25 mm. An optical fiber was placed in the pipe, and the continuous borehole temperatures can be obtained at a spatial resolution of 0.4 m along the fiber using the DTS (Okazaki et al., 2021). As the accuracy of PT100 decreases with wire length, PT100 is employed to measure the ground temperature within 30 m and at an interval of 1 m. The measurement precision of the DTS is 0.5 °C, while that of PT100 is 0.1 °C. Therefore, the latter with a higher accuracy was used to calibrate the temperatures acquired by the former.

2.3. Satellite temperature data

To acquire large-scale surface temperatures conveniently, land surface temperatures from the MODIS Collection-6 LST products were downloaded from http://earthdata.nasa.gov/. Nanjing is located at the tile of h28v05, and all the data of the sites were extracted from the district. The spatial resolution of the data is 1 km × 1 km. The data includes the temperatures at approximately 10:30 and 13:30 during daytime (Terra data) and approximately 22:30 and 01:30 during nighttime (Aqua data), respectively for the past ten years. Since satellite data can only be obtained under clear weather conditions, there will be a lack of temperature data. The S-G smoothing algorithm, a polynomial smoothing algorithm based on the least square principle proposed by Savizkg and Golay (Chen et al., 2004), has a higher reliability, thus it is applied to complete the missing data in this paper (Cao et al., 2018; Huang et al., 2020).

2.4. Calculation of subsurface temperatures

The in situ subsurface temperature monitoring process is usually very costly. Numerical simulations may provide the possibility of large-scale field monitoring at less cost. Based on layered thermal-physical features with the monitoring temperatures, a rapid estimation of future changes in subsurface temperatures can be realized. Here, the one-dimensional (1D) heat conduction equation is applied to acquire the subsurface temperatures. Because the permeability of the soil is small, thermal convection due to the groundwater flow is not considered (Taniguchi, 1993). To acquire the subsurface temperature variations and simplify the calculation, the following assumptions are made: (1) each soil layer is a homogeneous medium and isotropic; (2) groundwater flow is neglected; and (3) thermal dispersion is ignored. The one-dimensional thermal conduction can be expressed as (Stallman, 1965):

$$\lambda \frac{\partial T^2}{\partial z^2} = c\rho \frac{\partial T}{\partial t} \tag{1}$$

Initial condition:

$$T(z,t)|_{t=0} = T(z,0) \tag{2}$$

Boundary condition:

$$T(z,t)|_{z=0} = T(0,t), T(z,t)|_{z=\mathrm{D}} = T_0 \tag{3}$$

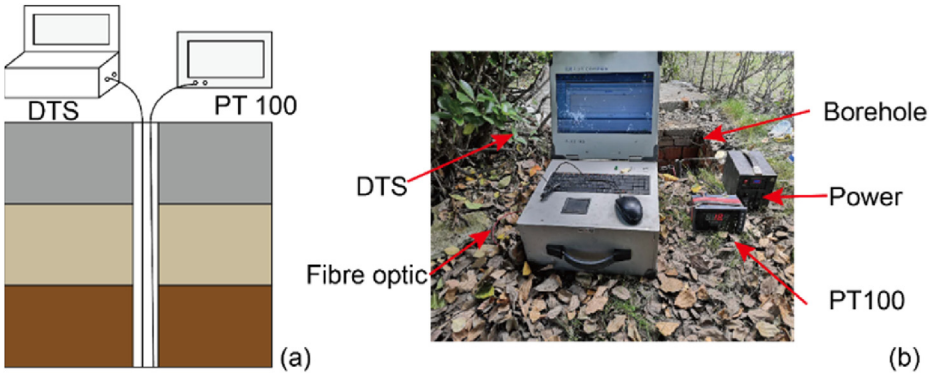

Fig. 3. Field monitoring and instrument diagram: (a) represents the schematic diagram of temperature measurement, and (b) represents the DTS monitoring in the field.

where T is the temperature (°C); z is the position in the subsurface(m); t is the time (s); λ is the bulk thermal conductivity of the soil-water matrix (W(m °C)); and c and ρ represent the heat capacity (J/(m^3 k)) and density (kg/m^3) of the soil-water matrix, respectively. Numerical calculations were implemented in MATLAB to obtain the finite-difference approximation. The boreholes SG39 and SG0 are chosen as the representative sites, with the land cover types of grassland and concrete respectively. According to the drilling cores, the tested thermal properties of sites SG39 and SG0 in the laboratory are shown in Table 1.

The derived surface temperatures of large areas from satellites are applied as the boundary condition in the simulation. Since the MODIS temperature is affected by many factors, there is a difference between satellite temperatures and measured surface temperatures. Therefore, the top boundary temperatures are calculated from the near-surface MODIS temperatures. The bottom boundary has a constant temperature level at the depth of about 20 m, which can be obtained from the annual measured temperatures of the specific sites. The borehole consists of different layers, and the layered thermal-physical parameters are listed in Table 1. Besides, simulation time begins in July and ends in November and lasts for about 3 months. The measured subsurface temperatures of the boreholes in July are used as the initial condition. The calculating space and time intervals are 0.4 m and 1 h respectively.

2.5. Geothermal potential evaluation

To assess the geothermal potential, the theoretical geothermal potential (TGP) is applied in this study, which reflects the heat supply in theory under natural conditions. In this section, we aim to evaluate the theoretical geothermal potential and identify the additional geothermal energy generated as a result of the subsurface urban heat island effect. The theoretical geothermal potential can be calculated by the following equations (Hemmerle et al., 2022):

$$Q = c\rho dA\Delta T \tag{4}$$

where Q represents the TGP (TJ); d represents the layer thickness (m); ΔT is the temperature difference between local subsurface temperature and natural background temperature of 10 °C; and A represents the heat transfer area of the reservoir.

3. Results

3.1. Surface temperatures from field-monitoring and MODIS

3.1.1. Monitoring surface temperatures

The ambient surface temperatures of several monitoring points (SG0, SG09, SG14, SG26, SG27, SG28, SG33, SG39, SG44, SG49) were acquired for a whole year. To reflect the relationship between air and surface temperatures, the mean daily air temperatures are loaded from https://data.cma.cn/. The results suggest that both the air and surface temperature variations obey the feature of cosine distribution approximately. To describe the characteristics of surface temperatures and illustrate the relationship with the air temperatures, the temperature variations are approximately described by the harmonic function (Taylor and Stefan, 2009). Based on the measured surface temperatures, the average temperature T_0 and temperature variation amplitude A (with 95% confidence) throughout one year are given in Table 2.

As shown in Table 2, the average land surface temperatures are between 17.2 °C and 22 °C and show big differences for different sites. Air temperature variations are within the range of land surface temperatures. The amplitudes of air temperatures are 0.75 °C–4.5 °C higher than that of the surface temperatures. Additionally, surface temperatures of residential and industrial districts are generally higher than those of grassland and bare soil surface temperatures.

3.1.2. MODIS temperatures from satellite measurements

To demonstrate the practicability of the MODIS temperatures, comparisons between MODIS temperatures and the corresponding iButton temperatures under concrete (SG0) and grassland (SG39) surfaces from July 2019 to July 2020 are plotted in Fig. 4a and b, respectively. From the results, a relatively significant relationship between MODIS and measured temperatures can be observed, which is described by the liner function.

Despite the difference between MODIS data and the measured data, the significant linear correlation between the MODIS and measured temperatures proves the reliability of the MODIS data product. The corrected functions show that the slope values of the two boreholes are similar, but the inception value of concrete is larger than that of grassland. Additionally, the temperature differences between corrected and uncorrected MODIS data are described in Fig. 5. The corrected temperatures are about −1 °C-1.5 °C and 1.5 °C–3 °C higher than the uncorrected data for grassland and concrete respectively, which also suggests that the difference between measured and MODIS temperatures of concrete is larger than that of grassland. For concrete, the temperature differences ΔT are larger during warm days in comparison to the ΔT in cold days. For

Table 2
Average values and amplitudes of air and surface temperatures.

Borehole	Land cover	T_0 (°C)	$\|A\|$ (°C)
Air	–	17.5	12.2
SG09	1	18	10.3
SG33	1	19.8	10.3
SG44	1	19.8	9.4
SG0	1	21.8	11.5
SG27	2	17	10.6
SG49	2	17.2	8.7
SG28	2	17.3	10
SG14	2	17.5	8.8
SG26	2	17.6	7.9
SG39	2	18.9	10.7

Note: For the land cover, '1' represents the residential and industrial districts, and '2' represents the agricultural and open districts and green parks.

Table 1
Thermo-physical properties of boreholes SG39 and SG0.

Borehole	Depth (m)	Thermal conductivity (W/(m °C))	Heat capacity (kJ/(kg K))	Density (10^3 kg/m^3)
SG39	0–6	1.69	1.75	1.74
	6–10	1.73	1.78	1.78
	10–20	1.65	1.77	1.66
SG0	0–4	1.58	1.56	1.85
	4–6	1.68	1.78	1.72
	6–16	1.72	1.76	1.77
	16–20	1.84	1.88	1.55

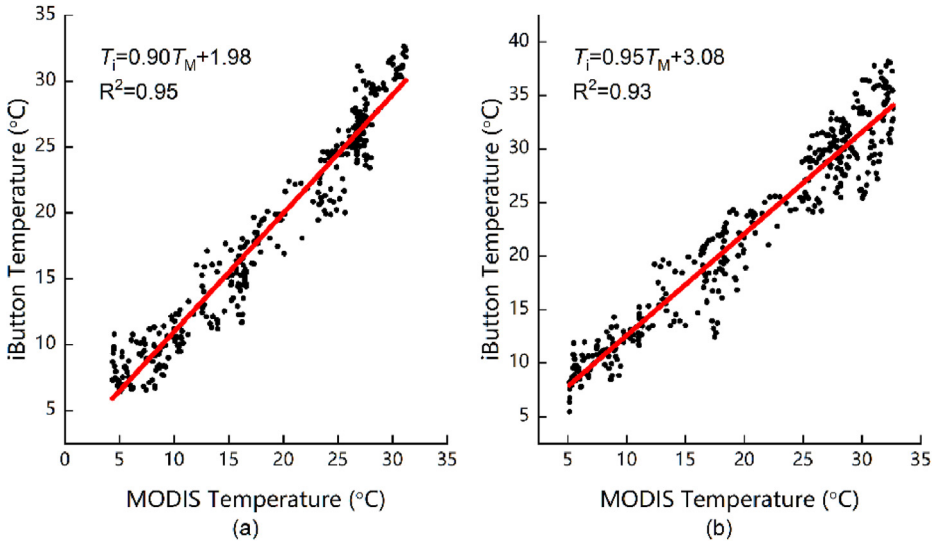

Fig. 4. (a) Correlation analysis of grassland between MODIS and iButton temperatures (SG39); and (b) Correlation analysis of concrete between MODIS and iButton temperatures (SG0).

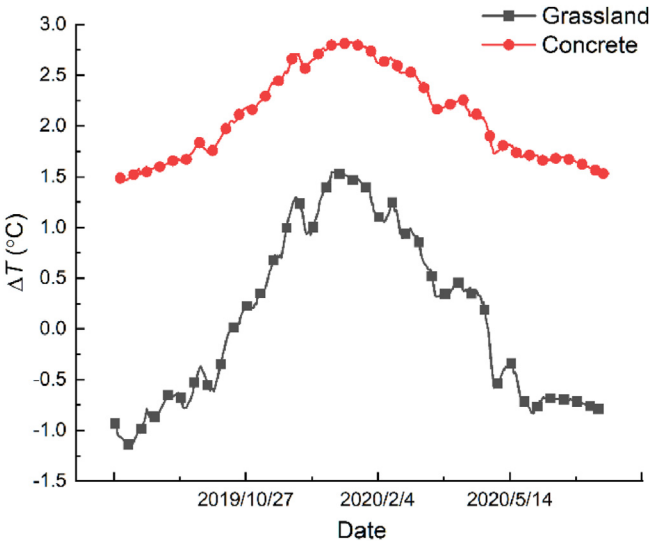

Fig. 5. Temperature difference Δ*T* before and after correcting MODIS temperatures for grassland and concrete throughout a year.

grassland, the corrected MODIS temperatures are higher than uncorrected temperatures on warm days, while the situation is contrary on cold days. Above all, the MODIS temperatures are effective in reflecting surface temperature distributions, and the precision of the data may be improved by field monitoring temperatures.

3.2. Field-monitoring results from the boreholes

Subsurface temperatures of these sites (SG03, SG19, SG26, SG27, SG39, SG45) were recorded through DTS in May 2019, August 2019, November 2019, and January 2020, which represent the subsurface temperature profiles in spring, summer, autumn, and winter. Some temperature-depth profiles of several boreholes observed in four seasons are depicted in Fig. 6. It can be seen that subsurface temperatures fluctuate widely between 0 m and 15 m for the seasonal variations. The depth range from 15 m to 20 m is usually regarded as the constant temperature zone. In this study, the depth of 20 m is regarded as the constant temperature-depth. Temperatures at 20 m below ground level of the districts are mostly concentrated in the range from 17.5 °C to 18.5 °C. In the following section, the measured temperatures will help verify the proposed subsurface temperature prediction model and evaluate shallow geothermal energy.

3.3. Comparison between measured and simulated subsurface temperatures

Simulated subsurface temperatures based on Eqs. (1)–(3) and measured subsurface temperatures at the same time are compared in Fig. 7. The simulated temperatures have a large consistency with the measured temperatures. The results indicate that the main difference between measured and simulated subsurface temperatures lies in the shallow depth of 0–3 m, under which the errors are mostly within 0.2 °C. Within the depth of 0–0.5 m, the near-surface temperature error can reach a maximum of 2 °C. With the increase in depth, the error keeps on a decreasing trend. Compared to the top boundaries with uncorrected MODIS temperatures, the simulated subsurface temperatures are closer to measured subsurface temperatures by using the corrected MODIS temperatures as a top boundary. The improved accuracy is different for grassland and concrete. For concrete, within the depth of 0.4–5.2 m, the accuracy of the simulated temperatures increased by 0.1 °C–3 °C. Meanwhile, for the grassland, the accuracy increased by 0.1 °C–0.2 °C at a depth of 0.4–3.6 m. Considering that the simulation time scale is relatively small (3 months), the improvement will be greater while predicting long-term temperature variations. Furthermore, by comparing subsurface temperatures under the two land surface types, subsurface temperatures below concrete are 1 °C–2.5 °C higher than subsurface temperatures below grassland at a depth of 0.8–8.4 m, and it is 0.5 °C–0.9 °C higher at a depth of 8.4–20 m. The difference reflects the effects the land surface has on the subsurface temperature distribution, to some extent. In conclusion, the method has good accuracy, which verifies the feasibility of the thermal conduction model.

3.4. Geothermal potential

According to the proposed TGP estimation method, the subsurface temperature variations throughout the whole year were acquired by the corrected MODIS temperatures as the boundary

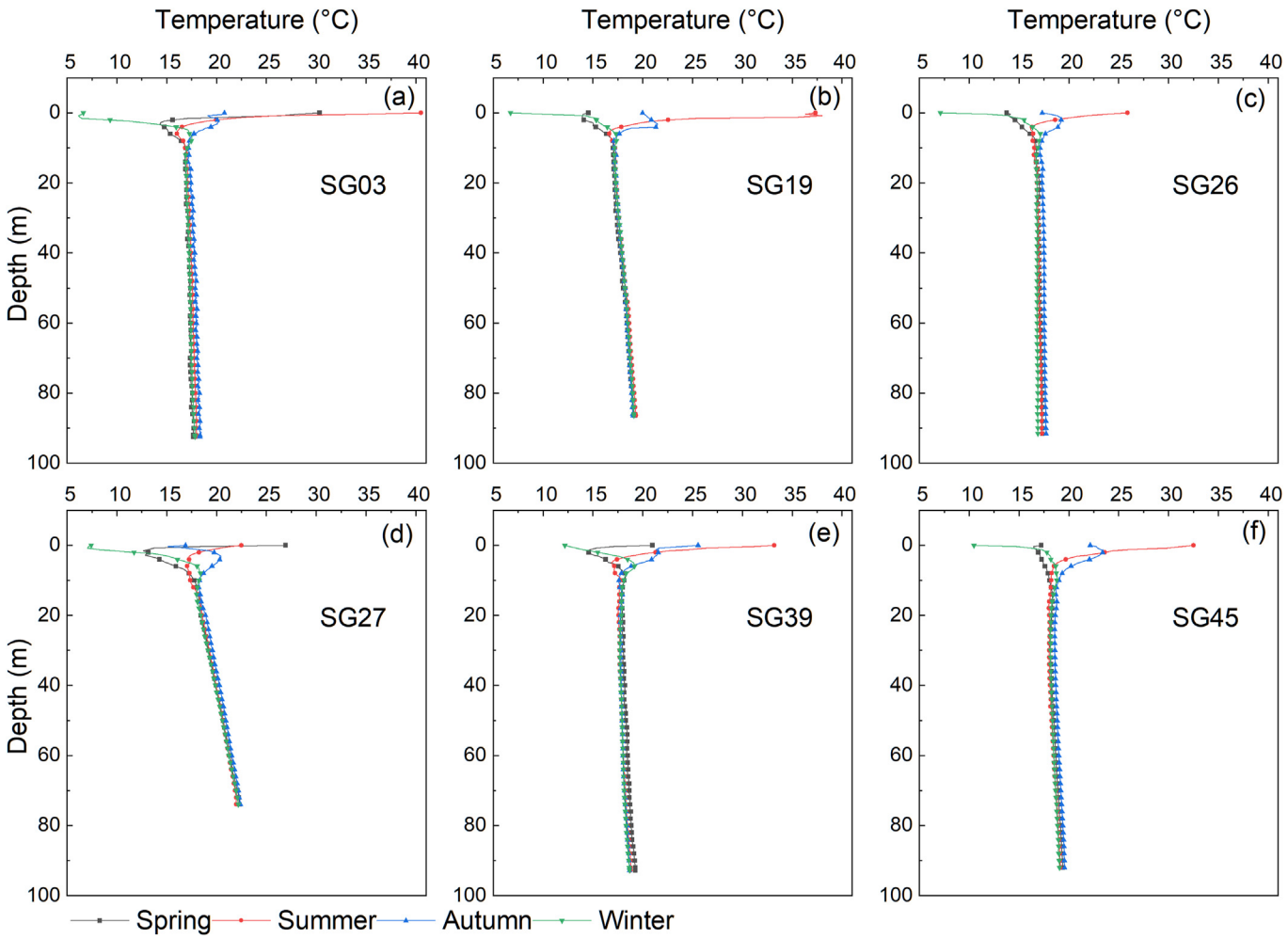

Fig. 6. Seasonal variations of subsurface temperatures at different sites; numbers represent the positions of boreholes.

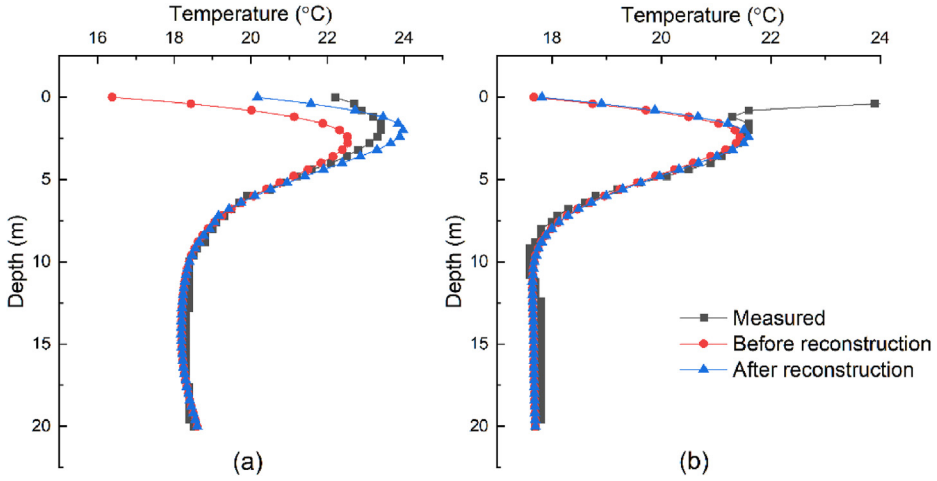

Fig. 7. Measured and simulated subsurface temperatures under different top temperature boundaries: (a) represents the borehole SG0 (concrete), and (b) represents the borehole SG39 (grassland).

conditions. To evaluate the UHI effect on the geothermal performance, boreholes SG0 and SG39 are selected to represent the temperature profiles of urban and rural areas respectively. The hourly temperature distributions them during the winter season (from December 1st to February 31st) are simulated, and the average TGP at different depths can be calculated based on Eq. (4).

The accumulated TGP at the reservoir depth of urban and rural areas is described in Fig. 8. At the same depth along the borehole,

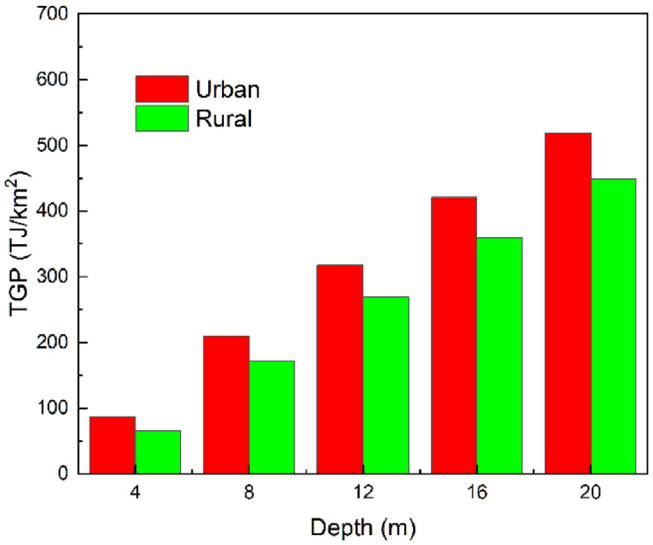

Fig. 8. Urban and rural TGPs under grassland and concrete.

there is an obvious difference between the urban and rural TGPs. When it reaches 20 m, the TGP of urban areas is 14.7% more than the TGP in rural areas, which suggests that the urban subsurface has more geothermal potential compared with rural areas.

4. Discussion

4.1. Effects on the temperature distribution

The temperature profiles have many differences in Fig. 6, the reasons can be attributed to many aspects. Previous studies indicate that temperatures are influenced by geological conditions, stratum lithology, and groundwater flow (Taylor and Stefan, 2009; Szijártó et al., 2019). In Fig. 6d, borehole SG27, which lies in the geothermal anomaly area, has a geothermal gradient of 6.74 °C. The drilling areas of SG03 and SG19 are both covered with thick unconsolidated sediments (Fig. 2), including sandy, gravelly, and other water-permeable soil layers. The two sites are close to surface water flow, so subsurface temperatures are relatively lower than other drillings (Fig. 6a and b). For borehole SG26, because of the existence of marlstone and sandy mudstone, karst water is widely distributed (Fig. 6c), which causes unstable ground temperature distribution. The results above suggest that the subsurface temperature variations are extremely complex under considerations of the geological and hydrological conditions of local sites.

Land cover is another important factor causing the deviation of the corrected model for surface temperatures. Surface temperatures depend on the thermal absorption ability and specific heat capacity of the land surface material (Taylor and Stefan, 2009). Grassland has a higher specific heat capacity while it has less heat absorption compared to concrete, so the surface temperatures of grassland cover are relatively lower. Additionally, the derived MODIS temperatures are close to the air temperatures (Roth et al., 2007), and concrete surface temperatures are generally higher than air temperatures (Table 1). Therefore, the surface temperatures of concrete are corrected more (1.5 °C–3 °C) than those of grassland (1 °C–1.5 °C). Air temperatures are generally lower in winter and higher in summer compared to the soil temperatures, so the corrected MODIS temperatures are much higher than the original data on cold days. Taking the above conditions into account, when the corrected MODIS temperatures were used as the top boundary, the modeling accuracy of the subsurface temperatures was improved more for concrete. For grassland, the difference in the temperature profiles between numerical and measured subsurface temperatures was smaller.

The land cover also influences the subsurface temperature distribution, which has been reported in other studies (Ferguson and Beltrami, 2006; Gunawardhana and Kazama, 2012; Rotta Loria et al., 2022). In this study, the thermal diffusivities can be calculated from the thermal physical parameters, and the results show that the thermal diffusivities are in the range of 0.55–0.65 m^2/s, so the geological condition has little effect on the subsurface temperatures. Hence, the difference in the subsurface temperature profiles can be largely attributed to the surface temperature distribution. The average surface temperatures of concrete are larger than that of grass, and more heat can be transferred below ground, so the subsurface temperature is also relatively higher. Above all, from the comparisons of the subsurface temperatures under grassland and concrete surfaces, it can be concluded that the land cover types affect both the surface temperature and the subsurface temperature distributions.

4.2. Limitations of subsurface temperature estimation approach

The model estimating the subsurface temperatures is under the assumptions in an ideal environment, while real subsurface temperatures are affected by many factors as illustrated in Section 4.1. However, the accuracy of the MODIS data and the land cover type are two main causes of the simulation.

On the one hand, as the top boundary, the MODIS temperatures after correction are still different from the real surface temperatures. That is because the MODIS data represents the average surface temperatures of one district, while iButton data represents the surface temperatures of one point in successive times. Aside from this, the MODIS temperatures are close to the air temperatures above the land surface, while the iButton data represents the surface temperature of several centimeters. The extracted MODIS temperatures are affected by weather and time of day (Brabyn et al., 2014). According to the temperature comparisons of SG09 at different times in Fig. 9, it can be recognized that the iButton data is higher than the corresponding nighttime MODIS data and lower than the daytime MODIS data. During the daytime, sunshine produces a mixture of shade and light districts and air temperature is usually greater, causing the MODIS temperatures to be higher. During the night, heat dissipates quickly and air temperature decreases rapidly. The accuracy of MODIS data during daytime and nighttime are not the same, but the corrected data are the average value during the day, so the difference between the two times of the day cannot be better distinguished. Consequently, it seems that the corrected method should consider more complicated factors to improve the accuracy of the corrected MODIS data.

On the other hand, the subsurface temperatures in the near subsurface are more sensitive to land cover type. From Fig. 7, the simulated surface temperatures are lower than the measured temperatures in the shallower layers within about 3 m subsurface. Grassland provides a more intense rainfall infiltration in comparison with concrete, whereby the water flow promotes heat transferring downward in the vertical tunnel. Besides, the collected borehole cores used to calculate the thermal-physical parameters may experience a water evaporation process, which reduces the moisture content of the testing samples. Higher moisture content increases the thermal conductivity of a formation (McDaniel et al., 2018). The shallow formation mainly includes silt and sand, and the moisture content of the soil is easily decreased during sampling, causing the tested thermal conductivity to decrease. Therefore, the

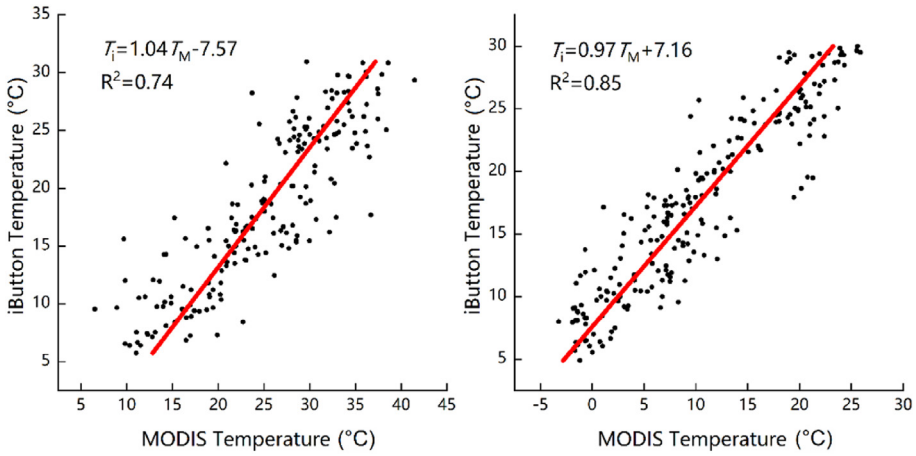

Fig. 9. (a): Correlation analysis of SG09 between MODIS and iButton temperatures during the daytime, and (b): correlation analysis of SG09 during the nighttime.

simulated subsurface temperatures with the land cover type of grassland are smaller than the measured temperatures at the shallower depths. While this is contrary for concrete, because of the imperviousness of this land surface, heat cannot be transferred into the subsurface effectively, which is why the simulated temperatures were higher.

A linear relationship between surface and MODIS temperatures seems not to consider some environmental factors, such as wind speed (Moazzam et al., 2022), rainfall (Huang et al., 2020), and snow (Jafarov et al., 2014). Besides, soil properties such as permeability and porosity are not considered in the empirical thermal conduction equation. Neglecting the effects of groundwater flow seems reasonable where groundwater activities are not so intense (Kurylyk et al., 2015). In addition, the presence of faults and fractures is not considered, which can also affect heat transfer and further affect the evaluation of geothermal energy. We recommend considering more factors in the model in future investigations.

4.3. Utilization of geothermal energy

In the present study, the corrected MODIS temperatures were used to derive subsurface temperatures, which can evaluate the real subsurface temperatures. The two representative boreholes have similar geological conditions, while the urban areas have more geothermal potential. The reason may be attributed to the UHI effect, under which subsurface temperatures of urban areas are higher than of rural areas. In the engineering practice of developing geothermal energy, the design and plan of ground source heat pump (GSHP) systems need to consider local conditions to optimize thermal performance. As shown in Fig. 8, more geothermal potential can be exploited with the increase of the underground depth. However, costs will multiply with an increase in drilling depth and number (Bayer et al., 2019). Thus, before exploiting geothermal energy, the geothermal potential can be evaluated by using the proposed method in this study. Furthermore, drilling costs could also be calculated based on the local geological conditions. Taking into account the local geothermal potential and the actual construction costs, an approximate design of a GSHP system can be facilitated. In addition, urban areas have greater heat storage compared with rural areas. Therefore, future geothermal energy development should be focused on urban areas, which could also reduce the UHI effect to some extent. The MODIS temperatures can help to evaluate the geothermal potential of one district at a low cost, which provides the basis for the development and installment of GSHP systems.

5. Conclusions

Based on the field survey of subsurface temperature distribution and the MODIS temperatures, relatively high-precision subsurface temperatures are obtained. The good agreement between field-monitoring temperatures and MODIS data shows that thermal remote sensing is an efficient and relatively reliable tool to obtain surface temperatures. Combined with the empirical thermal conduction equation, city-wide temperature distribution characteristics can be further detected.

When MODIS temperatures after correction are used as the top boundary condition, the simulated results agreed well with the measured temperature data below 3 m underground in three months. Compared with the direct use of satellite data as the upper boundary condition, the corrected MODIS data based on the proposed liner regression model improved the accuracy of 0.1 °C–3 °C at a depth of 0.4–5.2 m underground for the concrete, and 0.1 °C–0.2 °C within the depth of 0.4–3.6 m for the grassland. Besides, the land cover type also impacts the distribution of subsurface temperatures, with higher subsurface temperature differences of 0.5 °C–2 °C between concrete and grassland surfaces.

The accuracy of the subsurface temperature estimate method is influenced by many factors, including the influence of complex atmospheric conditions on satellite temperature accuracy, land surface heat absorption, and infiltration in shallower layers. Due to the subsurface UHI effects, the available TGP of urban areas is 14.7% more than that of rural areas.

In this study, based on a small amount of measured temperatures and MODIS temperatures, city-wide subsurface temperature distribution can be estimated. Future work could focus on the establishment of the specific relationship between surface temperatures and MODIS data, in considering local climate features and different land surface types. The derived geothermal field can be further used to assess the geothermal capacity and instruct the constructed position and mining depth of GSHP systems.

CRediT authorship contribution statement

Liwei Zhang: Conceptualization, Data curation, Methodology, Writing – original draft. **Chun Liu:** Conceptualization, Funding acquisition, Methodology, Project administration, Validation, Visualization. **Bin Shi:** Data curation, Supervision. **Peter Bayer:** Methodology. **Huan Geng:** Visualization, Writing – review & editing.

Declaration of competing interest

The authors declare that they have no known competing financial interests or personal relationships that could have appeared to influence the work reported in this paper.

Acknowledgment

Financial supports from the National Natural Science Foundation of China (Grant Nos. 42222707, 41761134089) are gratefully acknowledged. We thank Ryan Pearson for proofreading.

References

Ahmed, B., Kamruzzaman, M., Zhu, X., Rahman, M., Choi, K., 2013. Simulating land cover changes and their impacts on land surface temperature in dhaka, Bangladesh. Remote Sens 5 (11), 5969–5998.
Alcaraz, M., Garcia-Gil, A., Vazquez-Sune, E., Velasco, V., 2016. Advection and dispersion heat transport mechanisms in the quantification of shallow geothermal resources and associated environmental impacts. Sci. Total Environ. 543 (Pt A), 536–546.
Bae, S., Nam, Y., 2021. Comparison between experiment and simulation for the development of a tri-generation system using photovoltaic-thermal and ground source heat pump. Energy Build. 231, 110623.
Balugani, E., Lubczynski, M.W., Reyes-Acosta, L., van der Tol, C., Francés, A.P., Metselaar, K., 2017. Groundwater and unsaturated zone evaporation and transpiration in a semi-arid open woodland. J. Hydrol 547, 54–66.
Bayer, P., Attard, G., Blum, P., Menberg, K., 2019. The geothermal potential of cities. Renew. Sustain. Energy Rev. 106, 17–30.
Benz, S.A., Bayer, P., Goettsche, F.M., Olesen, F.S., Blum, P., 2016. Linking surface urban heat islands with groundwater temperatures. Environ. Sci. Technol. 50 (1), 70–78.
Benz, S.A., Bayer, P., Blum, P., 2017. Identifying anthropogenic anomalies in air, surface and groundwater temperatures in Germany. Sci. Total Environ. 584–585, 145–153.
Benz, S.A., Bayer, P., Blum, P., Hamamoto, H., Arimoto, H., Taniguchi, M., 2018. Comparing anthropogenic heat input and heat accumulation in the subsurface of Osaka, Japan. Sci. Total Environ. 643, 1127–1136.
Brabyn, L., Zawar-Reza, P., Stichbury, G., Cary, C., Storey, B., Laughlin, D.C., Katurji, M., 2014. Accuracy assessment of land surface temperature retrievals from Landsat 7 ETM + in the Dry Valleys of Antarctica using iButton temperature loggers and weather station data. Environ. Monit. Assess. 186 (4), 2619–2628.
Cao, R., Chen, Y., Shen, M., Chen, J., Zhou, J., Wang, C., Yang, W., 2018. A simple method to improve the quality of NDVI time-series data by integrating spatiotemporal information with the Savitzky-Golay filter. Remote Sens. Environ. 217, 244–257.
Chen, J., Jönsson, P., Tamura, M., Gu, Z., Matsushita, B., Eklundh, L., 2004. A simple method for reconstructing a high-quality NDVI time-series data set based on the Savitzky–Golay filter. Remote Sens. Environ. 91 (3–4), 332–344.
China Meteorological Data Network, 2019. http://data.cma.cn (Accessed 28 May 2024).
Des Tombe, B.F., Bakker, M., Smits, F., Schaars, F., Made, K.J., 2019. Estimation of the variation in specific discharge over large depth using distributed temperature sensing (DTS) measurements of the heat pulse response. Water Resour. Res. 55 (1), 811–826.
Dong, Y., McCartney, J.S., Lu, N., 2015. Critical review of thermal conductivity models for unsaturated soils. Geotech. Geol. Eng. 33 (2), 207–221.
Du, H., Wang, D., Wang, Y., Zhao, X., Qin, F., Jiang, H., Cai, Y., 2016. Influences of land cover types, meteorological conditions, anthropogenic heat and urban area on surface urban heat island in the Yangtze River Delta Urban Agglomeration. Sci. Total Environ. 571, 461–470.
Epting, J., Huggenberger, P., 2013. Unraveling the heat island effect observed in urban groundwater bodies – definition of a potential natural state. J. Hydrol. 501, 193–204.
Ferguson, G., Beltrami, H., 2006. Transient lateral heat flow due to land-use changes. Earth Planet Sci. Lett. 242 (1–2), 217–222.
Figura, S., Livingstone, D.M., Kipfer, R., 2015. Forecasting groundwater temperature with linear regression models using historical data. Ground Water 53 (6), 943–954.
Gunawardhana, L.N., Kazama, S., 2012. Using subsurface temperatures to derive the spatial extent of the land use change effect. J. Hydrol. 460–461, 40–51.
Hemmerle, H., Ferguson, G., Blum, P., Bayer, P., 2022. The evolution of the geothermal potential of a subsurface urban heat island. Environ. Res. Lett. 17 (8), 084018.
Herb, W.R., Janke, B., Mohseni, O., Stefan, H.G., 2008. Ground surface temperature simulation for different land covers. J. Hydrol. 356 (3–4), 327–343.
Huang, R., Huang, J.-x., Zhang, C., Ma, H.-y., Zhuo, W., Chen, Y.-y., Zhu, D.-h., Wu, Q., Mansaray, L.R., 2020. Soil temperature estimation at different depths, using remotely-sensed data. J. Integr. Agric. 19 (1), 277–290.
Jafarov, E.E., Nicolsky, D.J., Romanovsky, V.E., Walsh, J.E., Panda, S.K., Serreze, M.C., 2014. The effect of snow: how to better model ground surface temperatures. Cold Reg. Sci. Technol. 102, 63–77.
Kurylyk, B.L., McKenzie, J.M., MacQuarrie, K.T.B., Voss, C.I., 2014a. Analytical solutions for benchmarking cold regions subsurface water flow and energy transport models: one-dimensional soil thaw with conduction and advection. Adv. Water Resour. 70, 172–184.
Kurylyk, B.L., MacQuarrie, K.T.B., McKenzie, J.M., 2014b. Climate change impacts on groundwater and soil temperatures in cold and temperate regions: implications, mathematical theory, and emerging simulation tools. Earth Sci. Rev. 138, 313–334.
Kurylyk, B.L., MacQuarrie, K.T.B., Caissie, D., McKenzie, J.M., 2015. Shallow groundwater thermal sensitivity to climate change and land cover disturbances: derivation of analytical expressions and implications for stream temperature modeling. Hydrol. Earth Syst. Sci. 19 (5), 2469–2489.
Lesperance, M., Smerdon, J.E., Beltrami, H., 2010. Propagation of linear surface air temperature trends into the terrestrial subsurface. J. Geophys. Res. 115, D21115.
Li, L., Zha, Y., 2019. Satellite-based regional warming hiatus in China and its implication. Sci. Total Environ. 648, 1394–1402.
Li, K., Chen, Y., Wang, M., Gong, A., 2019. Spatial-temporal variations of surface urban heat island intensity induced by different definitions of rural extents in China. Sci. Total Environ. 669, 229–247.
Lin, Y., Wang, H., Hu, P., Yang, W., Hu, Q., Zhu, N., Lei, F., 2020. A study on the optimal air, load and source side temperature combination for a variable air and water volume ground source heat pump system. Appl. Therm. Eng. 178, 115595.
McDaniel, A., Fratta, D., Tinjum, J.M., Hart, D.J., 2018. Long-term district-scale geothermal exchange borefield monitoring with fiber optic distributed temperature sensing. Geothermics 72, 193–204.
Moazzam, M.F.U., Doh, Y.H., Lee, B.G., 2022. Impact of urbanization on land surface temperature and surface urban heat Island using optical remote sensing data: a case study of Jeju Island, Republic of Korea. Build. Environ. 222, 109368.
Mortimer, L., Aydin, A., Simmons, C.T., Love, A.J., 2011. Is in situ stress important to groundwater flow in shallow fractured rock aquifers? J. Hydrol. 399 (3–4), 185–200.
Okazaki, T., Kuramitz, H., Watanabe, T., Ueda, A., 2021. Scale sensor: rapid monitoring of scale deposition and inhibition using fiber optics in a geothermal system and comparison with other monitoring devices. Geothermics 93, 102069.
Popiel, C.O., Wojtkowiak, J., 2013. Temperature distributions of ground in the urban region of Poznan City. Exp. Therm. Fluid Sci. 51, 135–148.
Rivera, J.A., Blum, P., Bayer, P., 2015. Analytical simulation of groundwater flow and land surface effects on thermal plumes of borehole heat exchangers. Appl. Energy 146, 421–433.
Roth, M., Oke, T.R., Emery, W.J., 2007. Satellite-derived urban heat islands from three coastal cities and the utilization of such data in urban climatology. Int. J. Rem. Sens. 10 (11), 1699–1720.
Rotta Loria, A.F., Thota, A., Thomas, A.M., Friedle, N., Lautenberg, J.M., Song, E.C., 2022. Subsurface heat island across the Chicago Loop district: analysis of localized drivers. Urban Clim. 44, 101211.
Siler, D.L., Faulds, J.E., Hinz, N.H., Dering, G.M., Edwards, J.H., Mayhew, B., 2019. Three-dimensional geologic mapping to assess geothermal potential: examples from Nevada and Oregon. Geoth. Energy 7, 1–32.
Stallman, 1965. Steady One-Dimensional Fluid Flow in a Semi-Infinite porous medium with sinusoidal surface temperature. J. Geophys. Res. 70, 2821–2827.
Szijártó, M., Galsa, A., Tóth, Á., Mádl-Szőnyi, J., 2019. Numerical investigation of the combined effect of forced and free thermal convection in synthetic groundwater basins. J. Hydrol. 572, 364–379.
Taniguchi, M., 1993. Evaluation of vertical groundwater fluxes and thermal properties of aquifers based on transient temperature-depth profile. Water Resour. Res. 29, 2021–2026.
Taniguchi, M., Uemura, T., Sakura, Y., 2005. Effects of urbanization and groundwater flow on subsurface temperature in three megacities in Japan. J. Geophys. Eng. 2 (4), 320–325.
Taniguchi, M., Shimada, J., Fukuda, Y., Yamano, M., Onodera, S., Kaneko, S., Yoshikoshi, A., 2009. Anthropogenic effects on the subsurface thermal and groundwater environments in Osaka, Japan and Bangkok, Thailand. Sci. Total Environ. 407 (9), 3153–3164.
Taylor, C.A., Stefan, H.G., 2009. Shallow groundwater temperature response to climate change and urbanization. J. Hydrol. 375 (3–4), 601–612.
Tissen, C., Menberg, K., Benz, S.A., Bayer, P., Steiner, C., Götzl, G., Blum, P., 2020. Identifying key locations for shallow geothermal use in Vienna. Renew. Energy 167, 1–19.
Wang, Y., Zhang, F., Liu, F., 2023. Thermo-hydro-mechanical (THM) coupled simulation of the land subsidence due to aquifer thermal energy storage (ATES) system in soft soils. J. Rock Mech. Geotech. Eng. 16 (6), 1952–1966.
Yao, R., Wang, L., Huang, X., Niu, Z., Liu, F., Wang, Q., 2017. Temporal trends of surface urban heat islands and associated determinants in major Chinese cities. Sci. Total Environ. 609, 742–754.
Zhan, W., Zhou, J., Ju, W., Li, M., Sandholt, I., Voogt, J., Yu, C., 2014. Remotely sensed soil temperatures beneath snow-free skin-surface using thermal observations from tandem polar-orbiting satellites: an analytical three-time-scale model. Remote Sens. Environ. 143, 1–14.
Zhang, Y., Hao, S., Yu, Z., Fang, J., Zhang, J., Yu, X., 2018. Comparison of test methods for shallow layered rock thermal conductivity between in situ distributed thermal response tests and laboratory test based on drilling in northeast China. Energy Build. 173, 634–648.

Zhou, Y., Fox, G.A., Miller, R.B., Mollenhauer, R., Brewer, S., 2018a. Groundwater flux estimation in streams: a thermal equilibrium approach. J. Hydrol. 561, 822–832.
Zhou, D., Bonafoni, S., Zhang, L., Wang, R., 2018b. Remote sensing of the urban heat island effect in a highly populated urban agglomeration area in East China. Sci. Total Environ. 628–629, 415–429.
Zhu, K., Blum, P., Ferguson, G., Balke, K.-D., Bayer, P., 2010. The geothermal potential of urban heat islands. Environ. Res. Lett. 5 (4), 044002.
Zou, Z., Yan, C., Yu, L., Jiang, X., Ding, J., Qin, L., Wang, B., Qiu, G., 2021. Impacts of land use/land cover types on interactions between urban heat island effects and heat waves. Build. Environ. 204, 108138.

Liwei Zhang obtained his BSc in geological engineering from China University of Geosciences, and MSc degree in geological engineering from Nanjing University. Now he is a PhD student in Civil Engineering in Hongkong University of Science and Technology. His current research includes urban heat island effects, development of shallow geothermal energy, urban climate.